Gravity waves mapped by the OMEGA/MEX instrument through O-2 dayglow at 1.27 mu m: Data analysis and atmospheric modeling

Francesca Altieri, Aymeric Spiga, Ludmila Zasova, Giancarlo Bellucci, Jean-Pierre Bibring

Gravity waves mapped by the OMEGA/MEX instrument through O_2 dayglow at 1.27 μm: Data analysis and atmospheric modeling

Francesca Altieri,[1] Aymeric Spiga,[2] Ludmila Zasova,[3,4] Giancarlo Bellucci,[1] and Jean-Pierre Bibring[5]

Received 16 February 2012; revised 18 May 2012; accepted 18 May 2012; published 29 June 2012.

[1] We present the occurrence of waves patterns on the southern polar region of Mars as traced by the O_2 dayglow emission at λ = 1.27 μm during late winter/early spring of MY 28. The observations were carried out by the OMEGA (Observatoire pour la Minéralogie, l'Eau, les Glaces et l'Activité) imaging spectrometer on board Mars Express (MEX). Waves are found preferentially at high incidence angles and latitudes between 55° and 75°S. The dayglow intensity fluctuations are of the order of ±3% at incidence angle <88.5° and they can be explained by the propagation of gravity waves in the Martian atmosphere. Mesoscale meteorological modeling predicts gravity wave activity in the same range of latitude as the observed $O_2(a^1\Delta_g)$ wave patterns with temperature oscillations consistent with existing measurements. Moreover, gravity waves simulated through mesoscale modeling can induce dayglow fluctuations of the same order-of-magnitude as observed in the OMEGA maps. This study confirms that airglow imagery is a powerful method to detect and study the bi-dimensional propagation of gravity waves, as foreseen in previous studies coupling photochemical and dynamical models.

Citation: Altieri, F., A. Spiga, L. Zasova, G. Bellucci, and J.-P. Bibring (2012), Gravity waves mapped by the OMEGA/MEX instrument through O_2 dayglow at 1.27 μm: Data analysis and atmospheric modeling, *J. Geophys. Res.*, *117*, E00J08, doi:10.1029/2012JE004065.

1. Introduction

[2] Since the 1950s the detection of terrestrial atmospheric waves through the fluctuation in the nightglow intensities they can induce has been well documented [*Bertheir*, 1956; *Krassovsky*, 1957]. When the OH(4,1) band intensity oscillations and rotational temperatures were, for the first time, correlated with periods and phase speed expected for gravity waves [*Krassovsky*, 1972], nightglow emission variations began to be commonly attributed to them [e.g., *Tarasick and Hines*, 1990, and references therein]. Gravity waves (hereafter GWs) are mesoscale atmospheric oscillations related to the buoyancy restoring force, which play a key role in the circulation of planetary atmospheres. On Earth, vertically propagating GWs originate in the lower part of the atmosphere by a variety of mechanisms involving topography, fronts, convective cells, jet streams, wind shears and wave-wave interactions [e.g., *Fritts et al.*, 2006; *Spiga et al.*, 2008, and reference therein]. In the 1970s, Mariner 9 and Viking missions revealed that GWs are ubiquitous in the Martian atmosphere too [e.g., *Pickersgill and Hunt*, 1981] and the crucial role of GWs in transporting energy and influencing the synoptic circulation of the terrestrial planets has been acknowledged [*Barnes*, 1990]. Characteristics and sources of GWs remain, however, to be further assessed on Mars, both through original observational methods and mesoscale modeling.

[3] Since their propagation produces fluctuations in the temperature and density fields, Martian GWs have been identified from orbit in thermal profiles by infrared spectrometry [*Briggs and Leovy*, 1974] and radio occultation [*Hinson et al.*, 1999; *Creasey et al.*, 2006a], as well as in density measurements by accelerometers during the spacecraft aerobraking phases [e.g., *Keating et al.*, 1998; *Creasey et al.*, 2006b; *Fritts et al.*, 2006]. Apart from cloud imagery by spacecraft orbiting Mars [*Pettengill and Ford*, 2000; *Wang and Ingersoll*, 2002], Martian GWs were seldom mapped. On the basis of photochemical model results, *Melo et al.* [2006] proposed imaging of airglow features for searching and mapping GWs in the Martian atmosphere

[1]IAPS, Istituto di Astrofisica e Planetologia Spaziali, INAF, Rome, Italy.
[2]Laboratoire de Météorologie Dynamique, Université Pierre et Marie Curie, Paris, France.
[3]IKI, Space Research Institute, Russian Academy of Sciences, Moscow, Russia.
[4]Moscow Institute of Physics and Technology, Dolgoprudnyy, Russia.
[5]IAS, Université Paris Sud, Orsay, France.

Corresponding author: F. Altieri, IAPS, Istituto di Astrofisica e Planetologia Spaziali, INAF, Via del Fosso del Cavaliere 100, IT-00133 Rome, Italy. (francesca.altieri@inaf.it)

0148-0227/12/2012JE004065

through an adaptation of the approach developed by *Swenson and Gardner* [1998] for the Earth.

[4] In this paper, we present the detection of oxygen dayglow oscillations on Mars Express/OMEGA maps retrieved in Martian southern polar regions in late winter/early spring according to the method described in *Altieri et al.* [2009]. We discuss the link between airglow oscillations and GW activity through theoretical considerations [*Swenson and Gardner*, 1998] and mesoscale modeling, using the model by *Spiga and Forget* [2009]. The formation of the $O_2(a^1\Delta_g)$ molecules through ozone photolysis is described in section 2. In this section we also report how the 1.27 μm oxygen emission is monitored by the OMEGA mapping spectrometer. The method followed to search for wave patterns in the data set is given in section 3, together with the description of the properties of the observed waves. The simple case of the propagation of a monochromatic GW in an isothermal and windless atmosphere is treated in section 4, while the results of mesoscale modeling carried out in the Martian southern polar regions are reported and discussed in section 5. Conclusions are drawn in section 6.

2. The Oxygen Dayglow

2.1. Background

[5] During the day, $O_2(a^1\Delta_g)$ excited molecules (also referred as O_2 singlet delta molecules) are produced by the photolysis of ozone with an efficiency of 90%:

$$O_3 + h\nu \rightarrow O_2(a^1\Delta_g) + O, 0.20 < \lambda < 0.31\ \mu m \qquad (1)$$

while in the night they are formed by the three-body reaction O + O + CO_2 [e.g., *Bertaux et al.*, 2012]. The reaction rate for (1) varies with the distance between Mars and the Sun. According to *Nair et al.* [1994] and *Novak et al.* [2002] it is of the order of 2.2×10^{-3} s^{-1} at perihelion and 1.5×10^{-3} s^{-1} at aphelion, while it increases up to 2.9×10^{-3} s^{-1} at aphelion [*Krasnopolsky and Bjoraker*, 2000; *Krasnopolsky*, 2003] by assuming the yield of $O_2(a_1\Delta_g)$ in photolysis of ozone equal to the yield of $O(^1D)$ as tabulated by *DeMore et al.* [1997]. This value is closer to the one found by *Sander et al.* [2003] who included in their calculations the spin-forbidden branches of the O_3 photolysis. It corresponds to 2.75×10^{-3} s^{-1} at aphelion and it is used also in the three-dimensional photochemical model of *Lefèvre et al.* [2004]. The radiative lifetime τ of the $O_2(a_1\Delta_g)$ molecules is 3880 s according to *Badger et al.* [1965] with an accuracy of 15%. Recent measurements have shown higher values: 6803 s [*Mlynczak and Nesbitt*, 1995], 4566 s [*Newman et al.*, 1999], and 4480 s [*Krasnopolsky*, 2003].

[6] The $O_2(a^1\Delta_g)$ molecules decay at the $X^3\Sigma_g$ fundamental state by radiating most of the photons at $\lambda = 1.27$ μm. De-activation can also occur through collisions with CO_2 molecules (quenching):

$$O_2(a^1\Delta_g) + CO_2 \rightarrow O_2(X^3\Sigma_g) + CO_2 \qquad (2)$$

The reaction rate k_q is $<2 \times 10^{-20}$ cm^{-3} $molecule^{-1}s^{-1}$ [*DeMore et al.*, 1997].

[7] In absence of other processes, the condition of photochemical balance becomes

$$\alpha[O_3] = [O_2(a^1\Delta_g)]/\tau + k_q[O_2(a^1\Delta_g)][CO_2] \qquad (3)$$

where square brackets indicate number density for a given species and α is the reaction rate of (1). The de-excitation mechanism through collisions is dominant for altitudes where $\tau\, k_q\, [CO_2] > 1$, depending on τ, and more strongly on the CO_2 concentration and k_q values. For example, for τ = 3880 s, atmospheric profiles from Viking missions and $k_q = 2 \times 10^{-20}$ cm^{-3} $molecule^{-1}s^{-1}$, quenching is the major mechanism for deactivation at altitudes h < 30 km [*Novak et al.*, 2002], while for $k_q = 1 \times 10^{-20}$ cm^{-3} $molecule^{-1}s^{-1}$ it is dominant for h <23 km [*Krasnopolsky and Bjoraker*, 2000].

2.2. The 1.27 μm Emission as Seen by OMEGA

[8] The OMEGA imaging spectrometer has been designed to study the composition of Martian soil and ices, as well as atmospheric properties [*Bibring et al.*, 2004]. Its instantaneous field of view (IFOV) is 1.2 mrad and corresponds to a spatial resolution that ranges between 0.36 and 7 km/pixel, depending on the position of the Mars Express spacecraft on its elliptical orbit. OMEGA has a spectral range of 0.35–5.1 μm covered by three spectral channels: VNIR (0.35–1.06 μm), SWIR (0.93–2.7 μm) and LWIR (2.6–5.1 μm) with a mean spectral resolution of ~15 nm. It can provide, for each pixel of the image, a spectrum sampled in 352 spectral channels. The 3D (x, y and λ) data products are usually referred as "cubes." In order to build the x direction of each cube (perpendicular to spacecraft ground track), the VNIR channel uses a 2D detector (CCD) and operates in a pushbroom mode: the total field of view of the slit (providing the x direction and corresponding to 8.8°) is recorded at the same instant along the CCD rows, while the CCD columns are used to record the dispersed spectrum (λ-dimension). The SWIR and LWIR ones, having a linear array sensor, work in a whiskbroom mode: the spectrum of each pixel along the slit is recorded individually on the linear sensor and the whole slit is scanned pixel by pixel thanks to a scanning mirror. For all the three spectral channels, the y direction is built through to the motion of the spacecraft. The integration time for each spectrum can be 50 or 100 ms for the VNIR channel and 2.5 or 5 ms for the other two channels. The signal-to-noise ratio S/N is >100 over the full spectral range. Each OMEGA cube is provided with an auxiliary file containing information, for every pixel of the hyperspectral image, about the latitude and the longitude, acquisition time, Solar Longitude (Ls), MOLA altimetry, emission angle e (i.e., the viewing zenith angle) and incidence angle i (i.e., the solar zenith angle), distance between Mars and the Sun as well as the distance between the probe and the planet.

[9] At the OMEGA spectral resolution the fine structure of the $O_2(a^1\Delta_g) \rightarrow X^3\Sigma_g$ transition lines is not resolved and most of the emission falls inside the spectral channel centered at 1.271 μm. Compared to SPICAM [*Bertaux et al.*, 2006, *Fedorova et al.*, 2006] and PFS [*Formisano et al.*, 2004], the other two spectrometers on board Mars Express able to measure the O_2 emission with a better spectral resolution, OMEGA presents the advantage of

Table 1. List of the OMEGA Cubes Used in This Study

Cube	LS Degree	DELTA (App.MR)	Horizontal Wavelength (km)
3908_0	170.654	2–4	100
3917_0	172.038	2–4	100
3935_0	174.822	-	-
3939_0	175.444	-	-
3944_0	176.225	1–3	80–100
3947_0	176.693	2–3	80–130
3953_0	177.633	1	50–80
3960_0	178.731	1–2	50–100
3961_0	178.889	1–2	70–100
3962_0	179.046	1–2	70–110
3966_0	179.676	2–4	70–100
3972_0	180.623	2–4	70–150
3974_0	180.940	1–2	60–90
3975_0	181.098	1	50–80
3978_0	181.575	1	50–70
3981_0	182.050	1	50–80

imaging capabilities, which allows for studying the 2D distribution of oxygen dayglow. At 1.27 μm, the OMEGA resolving power is of the order of 100, compared to 2200 of SPICAM and 6000 of PFS. However, both SPICAM and PFS have a larger IFOV of the order of 1° and 1.6° respectively. From OMEGA data, we can recover the 82.3% of the column integrated emission at 1.271 μm, defining the continuum by means of the adjacent spectral channels at 1.256 and 1.285 μm in order to minimize the spectral influence of minerals and ices. The continuum is also affected by CO_2 atmospheric bands and solar absorption lines. In order to take them into account, we follow the method proposed in *Altieri et al.* [2009]:

$$I_0 = I_{1.271\mu m} - I_c = \left[\mathrm{I/F}(1.271\ \mu\mathrm{m})/\mathrm{T_{atm,}}(1.271\ \mu\mathrm{m}) - 0.5 \times (\mathrm{I/F}(1.256\ \mu\mathrm{m})/\mathrm{T_{atm}}(1.256\ \mu\mathrm{m}) + \mathrm{I/F}(1.285\ \mu\mathrm{m})/\mathrm{T_{atm}}(1.285\ \mu\mathrm{m}))\right] \times \mathrm{F_{Sun}}(1.271\ \mu\mathrm{m}) \quad (4)$$

where I_0 is the column integrated intensity of the emission line from the continuum I_c in radiance units (W m^2 sr^{-1} μm^{-1}), I/F (λ) is the radiance factor, F_{Sun} (λ) is the incident solar flux and $T_{atm}(\lambda)$ is the atmospheric gas transmittance at the considered wavelength λ. $T_{atm}(\lambda)$ is derived by dividing an OMEGA spectrum taken at the base of Olympus Mons by one taken over the summit, assuming similar surface composition [e.g., *Langevin et al.*, 2005]. I_0 is then converted in Mega Rayleigh (MR, 1 R = 10^6 photons cm^{-2} s^{-1} $(4\pi\mathrm{ster})^{-1}$) the standard unit for column integrated emission (in the literature usually reported as $4\pi I$, I being the surface brightness):

$$4\pi I(MR) = 4\pi \times I_0/0.823 \times (hc/\lambda)^{-1} \times \Delta\lambda \times 10^{-12} \quad (5)$$

with $\Delta\lambda$ = 0.014 μm, λ = 1.27μm, h = Planck constant, c = speed of the light in vacuum. The 4π factor in equation (5) takes into account the fact that a spectrometer does not measure the emittance (number of photons emitted from the $O_2(a^1\Delta_g)$ excited molecules per second per cm^3, i.e., a flux also defined volume emission rates), but the intensity of the emission integrated along the line of sight (number of photons per second per cm^2 per steradian).

[10] In order to scale the derived values taken for each pixel of the image at a given incidence angle i and emission angle e to the vertical atmospheric column, we performed the air mass correction according to *Krasnopolsky* [2003]:

$$4\pi I = \frac{4\pi I_0}{\frac{1}{\mu} + 2\rho} \quad (6)$$

where $\rho = \frac{I_c}{F_{sun}\mu_0}$ is the reflectance for an individual spectrum, μ_0 is the cosine of the incidence angle and μ is the cosine of the emission angle. The correction is usually applied excluding data acquired at limb or close to the terminator, where the field of view of an instrument can be larger than the angular size of the source irregularities. For the OMEGA IFOV of 0.07° it works up to 89.9° but diverges for greater values, following the behavior of 1/cos(i). Since we detect waves also in the night side (i > 90°), in the following section we show the OMEGA maps of the oxygen dayglow column integrated intensity not corrected for the air mass. In this way we can have a better coverage of the GWs, without excluding the regions mapped after the terminator. Units are then apparent MR (App. MR).

3. Observations

[11] Following GW detections in isolated OMEGA nadir maps of the $O_2(a^1\Delta_g)$ emission at λ = 1.27 μm [*Zasova et al.*, 2006; *Spiga et al.*, 2007; *Altieri et al.*, 2009], a detailed method has been applied here for searching waves in the $O_2(a^1\Delta_g)$ OMEGA nadir maps. Horizontal profiles of the O_2 column integrated emission along the x and y directions of OMEGA maps have been obtained through binning the data in boxes 5 × 5 pixel wide. For each horizontal profile, we consider a wave detection when the following conditions occur: (1) presence of 2 local maxima and 2 local minima consecutively; (2) $O_2(a^1\Delta_g)$ emission intensity of the minima ≥ detection limit; (3) difference between the maxima and the minima ≥G_0 + 2 σ, where G_0 and σ are respectively the center and the sigma of the Gaussian fit applied to the histogram of the standard deviations of each 5 × 5 pixel box. The G_0 + 2 σ limit ranges between 1 and 2 App. MR, while the detection limit is of the order of 3–4 App. MR, only in the case of orbit 3953 it reaches 2 App. MR. Waves have been detected on the southern polar region during late winter/early spring Martian Year (MY) 28 in the Ls range between 170.7° and 182.1°, for a total of 16 OMEGA cubes (Table 1).

[12] In Figure 1 we show the mosaic of OMEGA orbits on the southern hemisphere where wave patterns appear. The acquisition time of each orbit is reported in Table 1 in terms of Ls (0.5° ≈ 1 Martian day). Every track shown in Figure 1 has been acquired by OMEGA in about 15 min, with a mean spatial resolution of 6 km/pixel. The wave amplitude ranges from 1 to 4 App. MR, starting from the OMEGA detection limit. The horizontal wavelengths of the waves range from 50 to 150 km, well above the mean OMEGA spatial resolution. Waves are detected in 87.5% of the selected cubes and seen preferentially at incidence angles >80°, crossing the terminator in the night side before progressively vanishing. $O_2(a^1\Delta_g)$ molecules are continuously formed in daytime by the photolysis of ozone, providing a background emission at 1.27 μm, the mapping thereof could reveal wave propagation. In nighttime $O_2(a^1\Delta_g)$ molecules can survive about 1 to 2 h according to published lifetime estimates

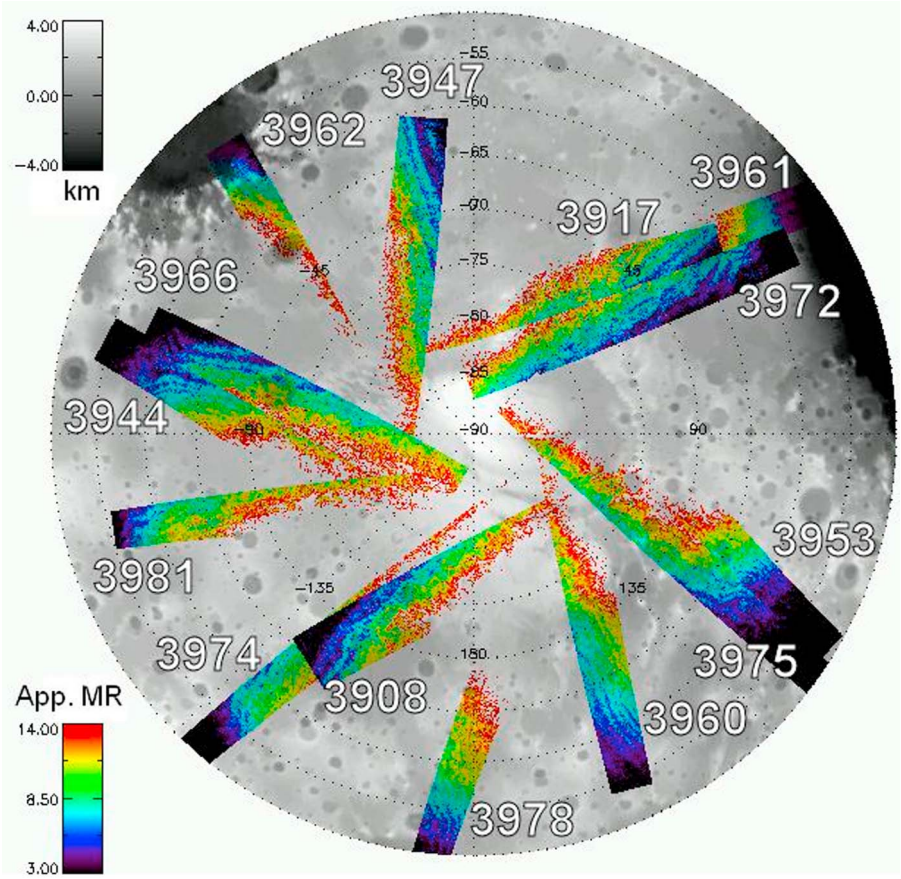

Figure 1. Mosaics of the OMEGA O_2 singlet delta column integrated emission maps showing waves superimposed on top the MOLA topography. O_2 singlet delta integrated intensities have been rescaled to the ones of orbit 3908 to have the same contrast. Values >14 app. MR are omitted. Cubes from orbit 3935 and 3939, not reported here, do not show evidence of waves (see also Table 1).

[*Badger et al.*, 1965; *Mlynczak and Nesbitt*, 1995]. Hence O_2 singlet delta molecules dayglow can trace wave occurrence in night side only at limited distance from the terminator, as is observed on OMEGA maps.

[13] In Figure 2 we show some of the $O_2(a^1\Delta_g)$ column integrated intensity maps overlaid on the MOLA topography. They are examples well representative of the different cases present in the whole considered data set. In some orbits, small-scale topography appears to play a role in shaping the wavefronts, as for orbit 3972, where the wavefronts, parallel to the terminator at higher latitude, appear perturbed by the crater in the upper right side of the image. In most orbits, however, the influence of small-scale topography on the wave signatures is not clear. This is the case of orbit 3953, where waves are transversal with respect to the terminator. Despite the fact that the wavefronts appear irregular, these small-scale irregularities are not correlated with the presence of highly cratered terrains. Finally, in case of orbit 3960, acquired over smoother regions, wavefronts are parallel to the terminator and remain not perturbed for a wide range of latitudes.

[14] In order to estimate the amplitude of the emission fluctuation, the $O_2(a^1\Delta_g)$ column integrated emissions have been corrected for the air mass. An example of the horizontal variations along a line perpendicular to the wavefront is reported in the upper panel of Figure 3 as a function of pixel number (mean latitude = −62°S, orbit 3953). At pixel 45, where the incidence angle reaches 90°, the curve drops down and then diverges. To evaluate the intensity of the fluctuations (clearly visible in the profile, continuum line), the unperturbed background has been fitted by a polynomial curve (dashed line). The ratio between the perturbed and unperturbed column integrated emissions is reported in the lower panel of Figure 3. The peak-to-peak fluctuations are of the order of 5–6% for incidence angles <88.5° and increase up to 10% and even more going forward to the terminator. The relative intensity is sensitive to the shape of the curve used to fit the continuum and this, together with the fact that in the night side the air mass correction cannot be applied, makes it difficult to evaluate if that trend is real or not. Hence, in the following analysis we assume an upper limit for the peak-to-peak dayglow fluctuation at 6%.

4. Atmospheric Response to GW Propagation

[15] *Melo et al.* [2006] and *Zhu and Yee* [2007] related airglow variations to the effect of the GW temperature fluctuations on the condensation of water vapor. Ozone, and thus $O_2(a^1\Delta_g)$, is anti-correlated with H_2O molecules, since HO_x compounds produced by their photolysis subtract the

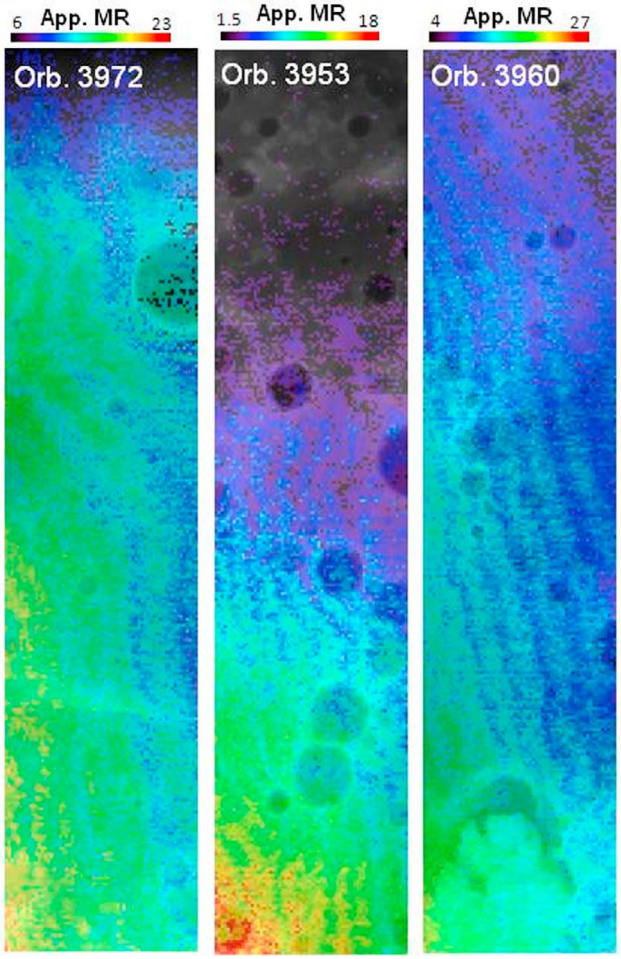

Figure 2. O_2 singlet delta column integrated emission maps for orbit 3972, 3953 and 3960 overlaid to the MOLA topography. Refer to Figure 1 for exact location.

odd oxygen needed for the recombination of the O_3. However, as in the considered season most of the water vapor is condensed on the southern polar cap, we do not expect this to play a key role in driving the observed dayglow fluctuations. Both OMEGA [*Maltagliati et al.*, 2011] and TES [*Smith*, 2004], the MGS Thermal Emission Spectrometer, measured water vapor values lower than 2 pr-μm. Assuming steady-state chemistry, a more likely mechanism to explain airglow fluctuations at high southern latitude during late winter/early spring is GW-induced perturbations in O_3 and CO_2 density profiles. To investigate this effect, before performing mesoscale modeling in the next section, we consider the simple case of a windless and isothermal atmosphere in which a monochromatic GW propagates with periods higher than O_3 chemical life time. O_3 chemical life time in equation (1) is given by the inverse of the reaction rate α and corresponds to about 5 min, assuming value for α proposed by *Sander et al.* [2003]. Since expected GW periods are typically over 1 h (this is confirmed by mesoscale modeling in section 5.2), we can thus adapt to the Martian atmosphere the theoretical framework of *Swenson and Gardner* [1998] describing the influence of GW on terrestrial OH airglow emission, as in *Melo et al.* [2006].

[16] Following this approach the relative atmospheric density fluctuation induced by a GW can be written as

$$\frac{\rho}{\rho_u} = \left[1 + \frac{\varepsilon}{(\gamma-1)} \times e^{\beta(z-z_{O3})} \times \cos[\omega t - kx + m(z-z_{O3})]\right]^{\gamma-1} \tag{7}$$

where

$$\rho_u(z) = \rho_u(0) \times e^{-z/H} \tag{8}$$

is the unperturbed density vertical profile for an isothermal atmosphere, H is the atmospheric scale height, $\rho_u(0)$ is the atmospheric density at the surface, z is the altitude, z_{O3} is the altitude of the peak of the O_3 layer, ε is the GW amplitude at z_{O3}, $1/\beta$ is the amplitude growth length ($1/\beta$ = 2H for undamped waves), ω is the intrinsic frequency, k is the horizontal wave number ($k = 2\pi/\lambda_h$ with λ_h = horizontal wavelength), m is the vertical wave number ($m = 2\pi/\lambda_z$ with λ_z = vertical wavelength) and γ is the ratio of specific heats.

[17] The horizontal and vertical wave numbers are linked to the intrinsic period through the GW dispersion relation:

$$m^2 = \frac{(N^2-\omega^2)}{(\omega^2-f^2)}k^2 \tag{9}$$

where compressibility term ($1/4H^2$) is neglected given typical values for scale height and GW vertical wavelength (cf. section 5.2). N and f are respectively the buoyancy frequency and the inertial frequency.

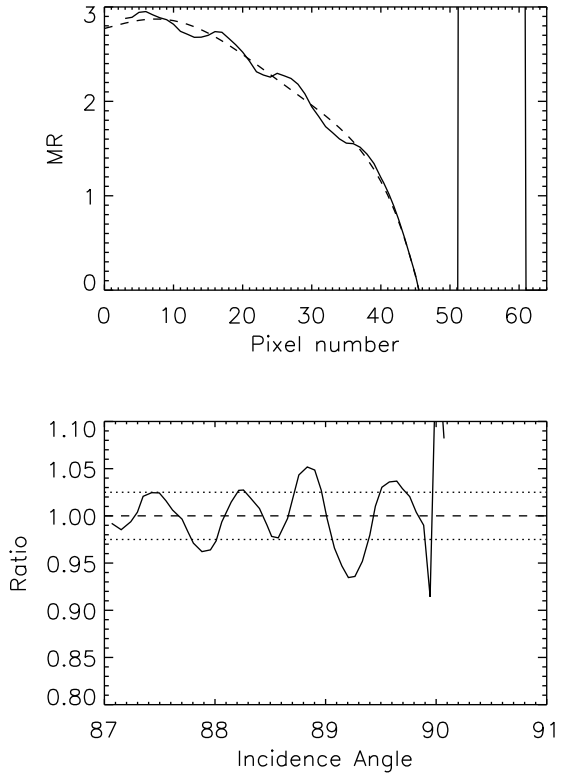

Figure 3. (top) $O_2(a^1\Delta_g)$ column integrated emission (orbit 3953) corrected for the air mass (continuum line) together with the fitted background (dashed line). (bottom) Ratio between the derived $O_2(a^1\Delta_g)$ intensity and the fitted background to evaluate the peak-to-peak absolute fluctuation.

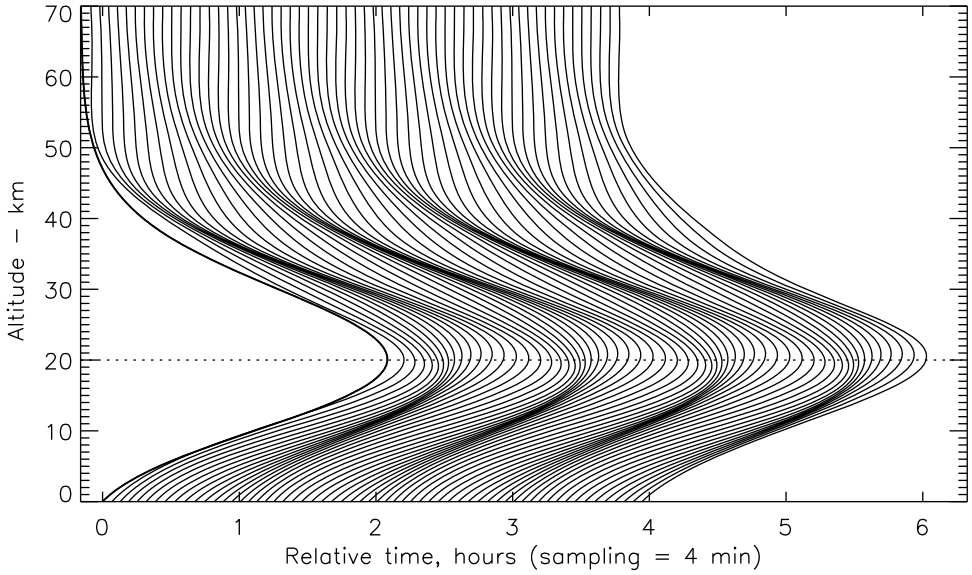

Figure 4. O_2 ($a^1\Delta_g$) volume emission rates as derived for τ = 5340 s, $\alpha = 3.1 \times 10^{-3}$ s^{-1} and $k_q = 2 \times 10^{-20}$ cm^{-3} $molecule^{-1}s^{-1}$. Thick line at time = 0: unperturbed profile. Thin lines: perturbed profile for ε = 2% and λ_Z = 30 km.

[18] The density variation for CO_2 and O_3 can be written, according to Swenson and Gardner [1998] as

$$\frac{[CO_2]}{[CO_2]_u} = \frac{\rho}{\rho_u} \tag{10}$$

$$\frac{[O_3]}{[O_3]_u} = \left(\frac{\rho}{\rho_u}\right)^{g_0(z)} \tag{11}$$

We fit the ozone vertical profile in the Martian atmosphere by an analytic curve of the form

$$[O_3]_u = f \times e^{\left[-(z-z_0)/H_1 - e^{-(z-z_0)/H_2}\right]} \tag{12}$$

The g_0 term has then the following expression:

$$g_0(z) = \frac{\gamma H - H_1}{(\gamma-1)H_1} - \frac{\gamma H}{(\gamma-1)H_2} \times e^{-(z-z_0)/H_2} \tag{13}$$

where z_0 = 26 km, H_1 = 5.4 km, H_2 = 15 km are the parameters to fit the O_3 density profile with a layer peaking at 10 km. For an ozone column integrated abundance of 1 μm-atm (1 μm-atm = 2.69×10^{15} molecule cm^{-2}) in equation (12) the value of f corresponds to 1.17×10^9 cm^{-3}. The ozone layer has been fitted comparing profiles derived from OMEGA limb data with ozone vertical distributions from *Krasnopolsky* [1982].

[19] The O_2 singlet delta perturbed vertical profiles are retrieved from equation (3), taking into account that the photo-dissociated ozone molecules produce molecular oxygen at $a^1\Delta_g$ excited state with an efficiency of 90%:

$$[O_2(a_1\Delta_g)]/\tau = \frac{\alpha \times 0.9 \times [O_3]}{(1 + \tau \times k_q \times [CO_2])} \tag{14}$$

Combining equations (10) and (11) with (14) we can also write:

$$[O_2(a_1\Delta_g)]/\tau = \frac{\alpha \times 0.9 \times \left(\frac{\rho}{\rho_u}\right)^{g0(z)} \times [O_3]_u}{\left(1 + \tau \times k_q \times \frac{\rho}{\rho_u} \times [CO_2]_u\right)} \tag{15}$$

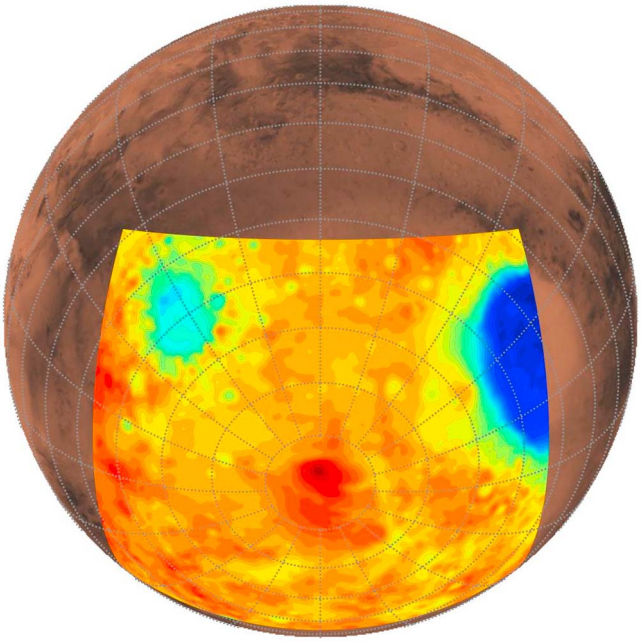

Figure 5. Domain set for mesoscale simulations carried out to resolved GW events in the Martian southern polar regions. The resolved topography is shown for the whole domain extent. The domain grid comprises 301 × 301 points with an horizontal resolution of 25 km. On the vertical dimension, 101 vertical levels are used up to 0.1 Pa and yields a vertical resolution of ~500 m.

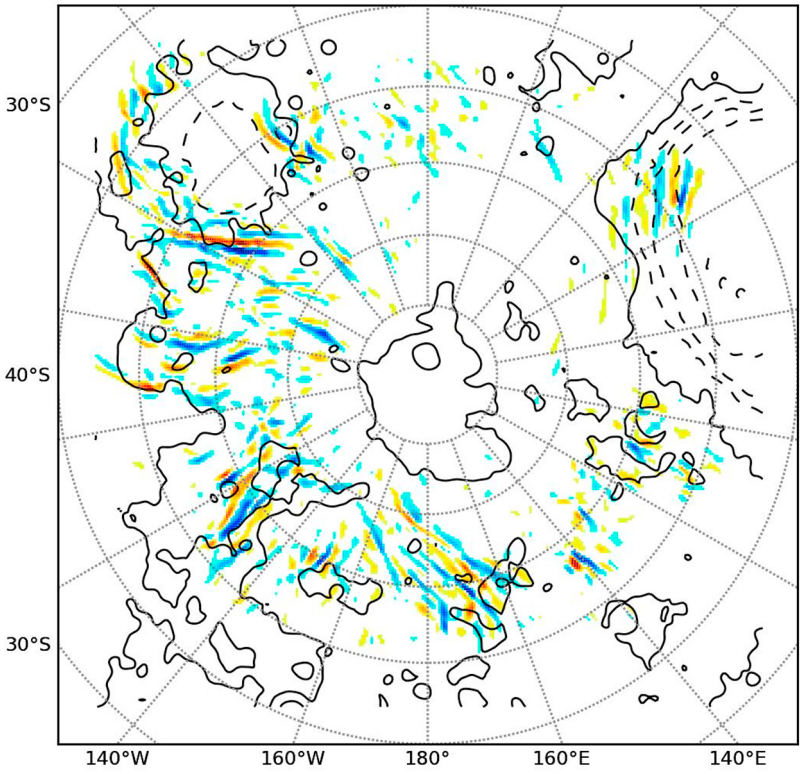

Figure 6. Predictions of the *Spiga and Forget* [2009] Martian mesoscale model for southern polar regions around spring equinox. Instantaneous vertical velocity fields on the 35 Pa isobar (∼25 km above the MOLA reference areoid) for the third day of simulation at universal time 2100 (i.e., local time at longitude 0°). Plotting with colors for vertical velocity is the following: it is omitted for values below 0.6 m s^{-1}, orange-red (blue) colors are used for positive (negative) values up to 4 m s^{-1} amplitude. Black contours indicate the topography of the southern polar regions each 2 km, black lines represent the downward short-wave flux at the surface (W m^{-2}) so as to describe the night/day areas.

where ρ/ρ_u is given by equation (7), $[CO_2]_u$ by equation (8), and $[O_3]_u$ by equation (12). Both reaction rates α and k_q are not function of the temperature [e.g., *Lefèvre et al.*, 2004; *DeMore et al.*, 1997].

[20] An example of the derived $O_2(a^1\Delta_g)$ volume emission rates is reported in Figure 4 for $\varepsilon = 2\%$ and $\lambda_Z = 30$ km, using for τ the intermediate value of 5340 s and assuming $\alpha = 3.1 \times 10^{-3}$ s^{-1} corresponding to the value in *Sander et al.* [2003] rescaled to the considered season, $k_q = 2 \times 10^{-20}$ cm^{-3} $molecule^{-1}s^{-1}$ (upper limit) and H = 8.3 km as derived by the fit of PFS spectra. In the data set used in this study, OMEGA is observing in nadir mode and what the instrument can measure are column integrated values. Hence for the sake of comparison, the vertical profiles of the $O_2(a^1\Delta_g)$ volume emission rates perturbed by GWs must be converted to column integrated quantities such as *I*. For plausible values of ε and λ_Z ($1\% < \varepsilon < 3\%$ and $10 < \lambda_Z < 50$ km), and taking into account the uncertainties of the other involved quantities (altitude of the ozone layer, atmospheric scale height, rate constants, radiative life time), it is possible to find peak-to-peak fluctuations in the ratio between the perturbed and unperturbed column integrated emissions as derived from equation (15) of the same order-of-magnitude of the ones observed in the OMEGA $O_2(a^1\Delta_g)$ dayglow maps. This indicates that the OMEGA airglow maps allow the instantaneous 2D monitoring of atmospheric gravity waves occurring in the Martian troposphere. We propose in the following section a more detailed assessment of this scenario through fine-scale atmospheric modeling.

5. Mesoscale Modeling

5.1. Methodology

[21] Owing to the spatial scale of the observed waves, the analogy with the terrestrial case and following estimates in the previous section, the OMEGA observed patterns in the 1.27 μm emission line appears to imply significant GW activity in the southern Martian polar regions. The detection of GW events through airglow can be compared to physically consistent numerical computations of the Martian atmospheric circulation through mesoscale modeling. Mapping airglow with OMEGA yields an unprecedented reference to validate the model, which in turn allows us to complement diagnostics derived from the observations.

[22] Limited area modeling at the mesoscale (i.e. <100 km grid spacing) with non-hydrostatic dynamics and polar stereographic projection is required to simulate the GWs underlying the $O_2(a^1\Delta_g)$ structures observed by OMEGA. General circulation models (GCMs) cannot resolve waves of horizontal wavelength below 300 km, necessitate numerical filtering in polar regions and generate a truncated GW

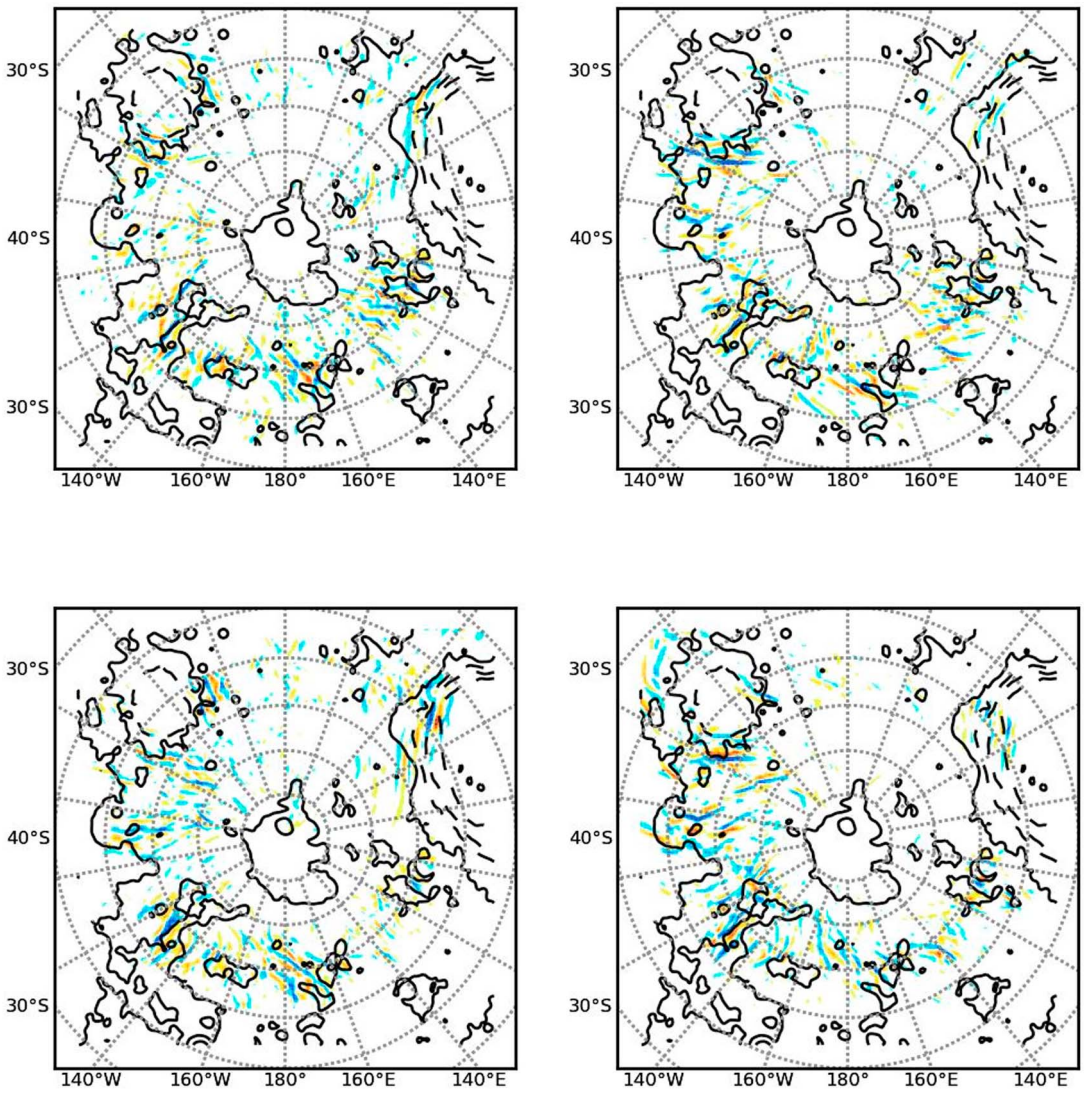

Figure 7. Same as Figure 6 but universal times (top left) 0600, (top right) 1200, (bottom left) 1800, and (bottom right) 0000 are shown.

spectrum owing to the hydrostatic assumption [*Fritts and Alexander*, 2003].

[23] In the present study, we use the Martian mesoscale model described in details in *Spiga and Forget* [2009] which couples fully compressible non-hydrostatic dynamics and comprehensive Martian physical parameterizations, while initial and boundary conditions are extracted from GCM simulations sharing same physical parameterizations [*Forget et al.*, 1999]. A few modifications were necessary to improve the accuracy of the mesoscale model for GW studies: (1) the model top is raised to 70 km (0.1 Pa) instead of usually 40 km (3 Pa); (2) a 3 × 3 smoothing window is applied to the model topographical field, to avoid spurious stationary patterns in vertical velocity triggered by "one-grid point" mountains or craters; (3) a GW "sponge layer" (diffusive damping) is activated between 55 and 70 km altitudes to prevent upward propagating GW to reflect back when reaching the model top [*Skamarock et al.*, 2008]. Following these changes, sensitivity tests were carried out to check consistency with the *Spiga and Forget* [2009] reference model.

[24] Domain settings are defined as a trade-off between large coverage of Martian southern polar regions and fine resolution of the GW signatures. A single polar stereographic domain is set, which grid is made of 301 × 301 horizontal grid points with 20 km spacing (Figure 5). In the vertical, 101 levels are set with average spacing of about 500 m between the top of boundary layer (where resolution is refined) and the bottom of sponge layer (where resolution is coarser). The effective resolution for GWs is 4 grid points: a minimum of 3 grid points to form a consistent wave signal and an additional grid point to account for the sharp drop-off of energy at the highest wave numbers caused by numerical filtering. Hence the mesoscale simulations performed here depict the gravity wave spectrum for wavelengths above 80 km (horizontal) and 2 km (vertical). Model is run at the season of OMEGA observations from sol 372 to sol 375 (Ls = 180° to 182°) with MY24 dust forcing [see *Montabone et al.*, 2005], typical of non-global dust storm conditions prevailing during MY28 OMEGA observations.

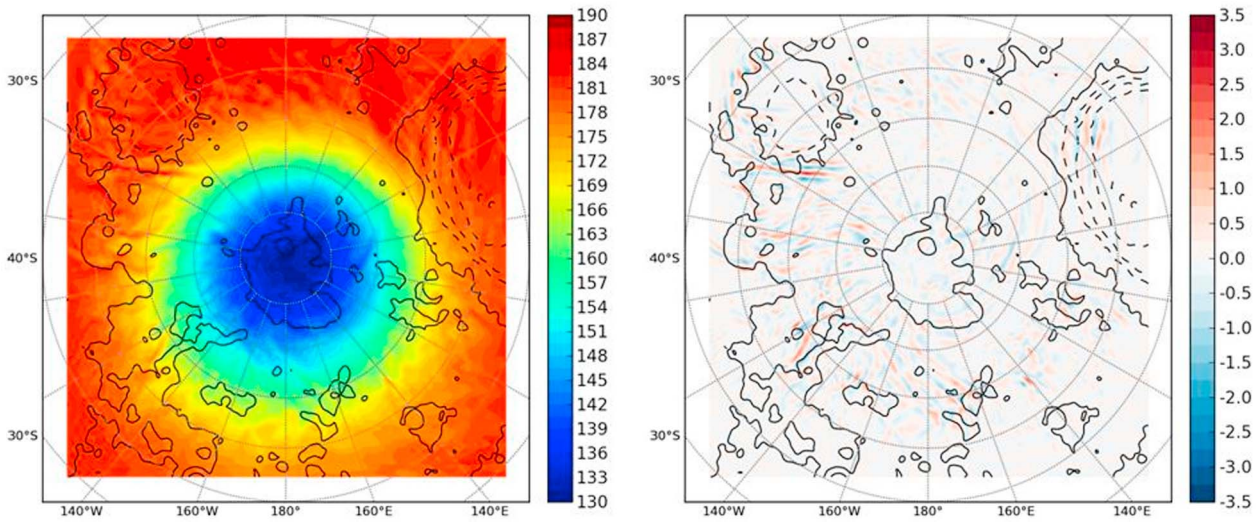

Figure 8. Predictions of the *Spiga and Forget* [2009] Martian mesoscale model for southern polar regions around spring equinox. (left) Instantaneous temperature field (K) on the 35 Pa isobar (∼25 km above the MOLA reference areoid) for the third day of simulation at universal time 2100 (similarly to Figure 6). (right) The corresponding relative variations of temperature are shown in %. The "average" large-scale temperature field is computed by applying a 10 × 10 smoothing window to the temperature field on the left (the estimates for wave signatures are not found to be sensitive to the choice of smoothing window as long as a grid greater than 8 × 8 is used). GW signatures in the temperature field are found in the same regions as vertical velocity signatures in Figure 6. Black contours indicate the topography of the southern polar regions each 2 km.

First day of simulation serves as model spin-up and is not retained for analysis.

5.2. GW Perturbations and Airglow

[25] The analysis of second to fourth days of the mesoscale simulation is in agreement with the scenario inferred from observations that spatial structures in the $O_2(a^1\Delta_g)$ dayglow maps are caused by GWs. Intense GW activity in Martian southern polar regions at any time of day is exemplified by instantaneous vertical velocity fields shown on the 35 Pa isobar (∼25 km above MOLA) in Figures 6 and 7. Most vertical velocity perturbations above 2 m s^{-1} are alternate patterns of negative and positive velocity related to the propagation of GWs. Corresponding structures are found in the horizontal wind divergence and potential temperature fields (not shown for the sake of brevity). Wavelengths of simulated wave packets are 120 to 250 km in the horizontal and 15 to 25 km in the vertical. The intrinsic period given by GW dispersion relationship is typically 2 to 3 h. Upward-propagating GW are characterized by coupled fluctuations of density, temperature, wind and pressure, which increase exponentially with altitude. For instance, *Fritts et al.* [2006] detected GW density fluctuations up to ±50% at an altitude of 100 km, while *Creasey et al.* [2006a] identified GW temperature fluctuations of the order ±2–4% at altitudes 20–30 km. This can be compared to Figure 8 which shows the predicted temperature field in the southern polar regions, as well as the relative fluctuations of temperature with respect to the average large-scale temperature field (note that on an isobar the relative temperature fluctuations are equivalent to the relative density fluctuations). At the locations where strong GW events occur (see Figure 6), the relative fluctuations of atmospheric temperature predicted by the mesoscale model reach ±3.5% at an altitude ∼25 km, giving further confidence that the mesoscale model is reproducing realistic GW events.

[26] The orientation and wavelength of simulated GW wavefronts in Figure 6 share similarities with the observed structure of dayglow oscillations caused by putative GW activity. The approach developed in section 4, based on the work by *Swenson and Gardner* [1998] and *Melo et al.* [2006] can help to go further than this mere qualitative comparison. Figure 9 shows an estimated map of the integrated airglow intensity, obtained through equation (15) using relative density fluctuations computed in the mesoscale model instead of the idealized monochromatic GW packet described in equation (7). The vertical integration is performed from above the boundary layer (5 km) toward the uppermost layer in the model where GW absorbing layer is not activated (55 km). Figure 3 confirms that the propagation of GW in the Martian mesosphere could imply detectable fluctuations of integrated airglow intensity. This also exemplifies how Martian airglow measurements could constrain predicted GW in meteorological models. The predicted peak-to-peak fluctuations of integrated airglow intensity for the most prominent GW events in the mesoscale simulations reach 3 to 5%, corresponding to typical values measured by the OMEGA spectrometer. It is important to note though that the estimates in Figure 9 should not be interpreted further than the order-of-magnitude level: equations (10), (11) and (13), hence (15), were derived in a simple theoretical framework considering a monochromatic GW packet in a windless isothermal case. Comparisons between modeling and observations at a higher level of

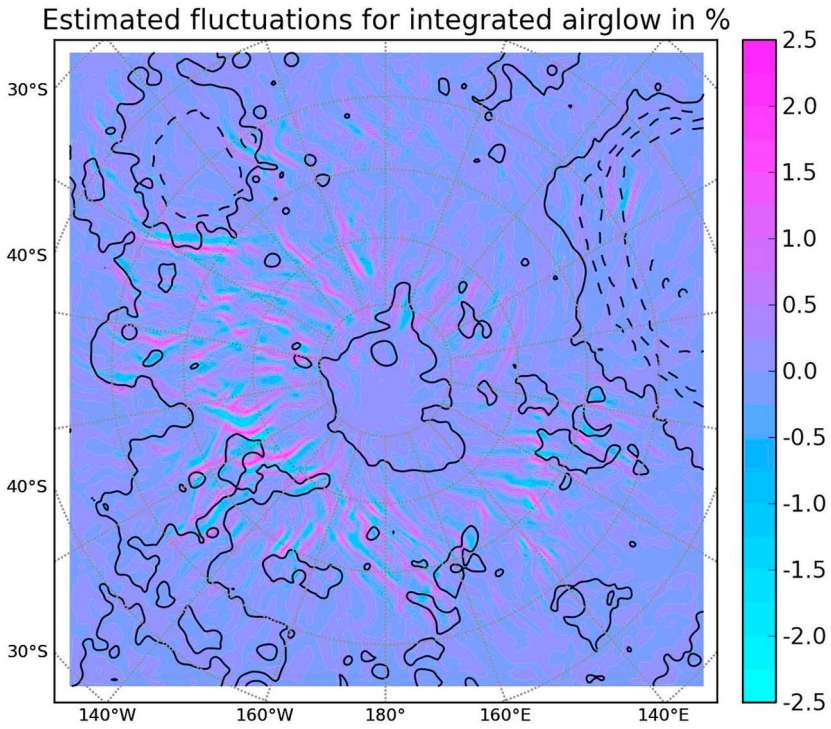

Figure 9. Estimated fluctuations of integrated airglow intensity in %, derived from predictions of the *Spiga and Forget* [2009] Martian mesoscale model for southern polar regions around spring equinox. This map is obtained (1) by computing vertical profiles of airglow intensity through applying equation (15) with relative density fluctuations computed in the mesoscale model for the third day of simulation at universal time 2100 (cf. Figure 8) and (2) by a vertical integration performed from above the boundary layer (5 km) toward the uppermost layer in the model where GW absorbing layer is not activated (55 km).

accuracy could be obtained through simulations coupling the mesoscale model with photochemistry computations, which are out of the scope of the present work.

5.3. GW Variability

[27] We can go a bit further in analyzing model predictions in order to complement diagnostics obtained through remote-sensing observations. Notably, the model helps to discuss spatial and temporal variability of GW activity in the Martian southern polar regions.

[28] The mesoscale model predicts a moderate diurnal variability of GW activity, as it can be inferred from Figure 7. No specific local time appears preferential for GW emission; the diurnal variability is caused instead by fluctuations of atmospheric stability and winds, and the impact thereof on GW propagation. In particular, GW activity is not especially enhanced in the vicinity of the terminator, where fluctuations of $O_2(a^1\Delta_g)$ emission are detected. Such preferential detection could be explained by better contrast for wave fluctuations at high incidence angle with respect to background signal.

[29] Reproducing the localization and structure of each observed wave is obviously not a reasonable project, given the unavailability of Martian measurements that could better constrain the mesoscale model. Yet it can be inferred from Figure 7 that GW activity is predominantly predicted at latitudes where most wave patterns are found in the OMEGA observations (Figure 1), i.e., between latitudes 55°S and 75°S. The intensity of GW events is decreasing at lower latitudes (below 50°S) and close to the pole (above 75°S). These results suggest that wave detection mostly at latitudes between 55°S and 75°S is not an observational bias but point out areas of prominent emission and favorable propagation conditions. Interestingly, the predicted GW activity is not evenly distributed over longitudes, showing e.g., enhanced activity in the vicinity of Hellas and Argyre craters and in Cimmeria and Sirenum plains. Though nearly each OMEGA wave event in Figure 1 roughly corresponds to longitudes where predicted GW activity is significant, the OMEGA coverage remains insufficient to further validate the longitudinal distribution of GW activity simulated by the mesoscale model.

[30] It is difficult to conclude unambiguously on the meteorological phenomena responsible for such (observed and predicted) latitudinal and longitudinal variability in GW activity. GW sources over a specific area remain difficult to determine, even in terrestrial studies (cf. references in *Spiga et al.* [2008]). Potential GW sources here include frontal activity, jet stream and topography. All those sources could be at play in the Martian southern polar regions at the end of winter.

[31] 1. Frontal activity through baroclinic instability is still strong around the spring equinox and yields a “storm track” in the vicinity of latitudes where GW activity is observed/predicted. This is further supported by the strong poleward temperature gradients (hence baroclinicity) at those latitudes in Figure 8 (left).

[32] 2. Though not the most prominent on Mars, topographical gradients are large in the considered region and may interact with strong low-level winds associated with the polar vortex.

[33] 3. Strong jet streams occur at these season and region, implying large accelerations and shears that could trigger GWs.

[34] In addition to GW sources, atmospheric large-scale conditions such as temperature and winds impact the GW propagation, hence GW activity [*Spiga et al.*, 2012, and references therein]. This illustrates the difficult task of explaining GW variability. For instance, jet streams impact GW activity both as a GW source and as a factor influencing GW propagation. Moreover, those large-scale jets are in turn perturbed by GW drag when waves become unstable at high altitudes and break. Additional GW measurements are needed before those questions could be addressed.

6. Conclusions

[35] We report on the detection of atmospheric wave patterns over southern polar regions during late winter/early spring thanks to imaging of the $O_2(a^1\Delta_g)$ dayglow by OMEGA/MEX. Waves appear preferentially at high incidence angles between 55° and 75°S and with spatial scales ranging from 50 to 150 km. The waves extend up to the night side, not allowing air mass correction to the whole OMEGA maps. The associated amplitudes vary between 1 and 4 MR in apparent units. Absolute intensity fluctuations are of the order of ±3% for incidence angles <88.5° and they seems to increase forward the night side. Uncertainty on the background intensity level and in the air mass correction do not allow to evaluate if this trend is real or not. We propose, as a possible mechanism explaining airglow fluctuations, GW-induced perturbations in the O_3 and CO_2 density profiles. This is supported through theoretical computations in an idealized framework. Mesoscale atmospheric modeling can also be employed to assess the validity of this inferred scenario. The mesoscale model confirms that southern polar regions during late winter/early spring are prone to intense GW activity at altitudes where O_2 emission is significant. The model shows a moderate diurnal variability of GW activity: the terminator, where waves are detected through O_2 emission, appears to play no prominent role in GW emission or propagation conditions. Significant GW activity is predicted in the latitude range where most wave patterns are observed. At first approximation the model is able to reproduce airglow fluctuations of the same order of the one observed in OMEGA maps. A higher level of accuracy could be reached by the coupling of the mesoscale model with photochemistry computations, considered as a future, much more sophisticated, development. Further observations by existing and future Martian missions are also needed to better constrain GW intensity and identify their sources.

[36] **Acknowledgments.** Authors are grateful to two anonymous reviewers for their constructive comments and suggestions. F.A. and A.S. thank L. Montabone and F. Lefèvre for useful discussions. Authors thank ASI, CNES and the Roscosmos for financing the OMEGA experiment and supporting this study. We are also grateful to the whole OMEGA team and ESA staff for scientific, operational and technical supports. F.A and G.B are thankful to ASI for the financial support through contract N. I/060/08/0. A.S. acknowledges support from ESA and CNES in the development of the LMD Martian Mesoscale Model. L. Z. acknowledges also support from the Russian Government grant to MIPT for the ISPAVR laboratory.

References

Altieri, F., L. Zasova, E. D'Aversa, G. Bellucci, F. G. Carrozzo, B. Gondet, and J.-P. Bibring (2009), O2 1.27 μm emission maps as derived from OMEGA/MEx data, *Icarus*, *204*, 499–511, doi:10.1016/j.icarus.2009.07.022.

Badger, R. M., A. C. Wright, and R. F. Whitlock (1965), Absolute intensities of discrete and continuous absorption bands of oxygen gas at 1.26 and 1.065 μm and radiative lifetime of the $^1\Delta_g$ state of oxygen, *J. Chem. Phys.*, *43*, 4345–4350, doi:10.1063/1.1696694.

Barnes, J. R. (1990), Possible effects of breaking gravity waves on the circulation of the middle atmosphere of Mars, *J. Geophys. Res.*, *95*, 1401–1421, doi:10.1029/JB095iB02p01401.

Bertaux, J.-L., et al. (2006), SPICAM on Mars Express: Observing modes and overview of UV spectrometer data and scientific results, *J. Geophys. Res.*, *111*, E10S90, doi:10.1029/2006JE002690.

Bertaux, J. L., B. Gondet, F. Lefèvre, J. P. Bibring, and F. Montmessin (2012), First detection of O2 1.27 mm nightglow emission at Mars with OMEGA/MEX and comparison with general circulation model predictions, *J. Geophys. Res.*, *117*, E00J04, doi:10.1029/2011JE003890.

Bertheir, P. (1956), Etude spectrophotométrique de la luminescence nocturne des bandes des molecules OH et O2 atmosphériques, *Ann. Geophys.*, *12*, 113.

Bibring, J.-P., et al. (2004), OMEGA: Observatoire pour la Minéralogie, l'Eau, les Glaces et l'Activité, in *Mars Express: The Scientific Payload*, edited by A. Wilson, *Eur. Space Agency Spec. Publ.*, *ESA SP-1240*, 37–49.

Briggs, G., and C. B. Leovy (1974), Mariner 9 observations of the Mars north polar hood, *Bull. Am. Meteorol. Soc.*, *55*, 278–296, doi:10.1175/1520-0477(1974)055<0278:MOOTMN>2.0.CO;2.

Creasey, J. E., J. M. Forbes, and D. P. Hinson (2006a), Global and seasonal distributions of gravity wave activity on Mars' lower atmosphere derived from radio occulation data, *Geophys. Res. Lett.*, *33*, L01803, doi:10.1029/2005GL024037.

Creasey, J. E., J. M. Forbes, and G. M. Keating (2006b), Density variability at scales typical of gravity waves observed in Mars' thermosphere by the MGS accelerometer, *Geophys. Res. Lett.*, *33*, L22814, doi:10.1029/2006GL027583.

DeMore, W. B., S. P. Sander, D. M. Golden, R. F. Hampson, M. J. Kurylo, C. J. Howard, A. R. Ravhankara, C. E. Kolb, and M. J. Molina (1997), *Chemical Kinetics and Photochemical Data for Use in Stratospheric Modeling*, Jet Propul. Lab., Pasadena, Calif.

Fedorova, A., O. Korablev, S. Perrier, J.-L. Bertaux, F. Lefevre, and A. Rodin (2006), Observation of O_2 1.27 μm dayglow by SPICAM IR: Seasonal distribution for the first Martian year of Mars Express, *J. Geophys. Res.*, *111*, E09S07, doi:10.1029/2006JE002694.

Forget, F., F. Hourdin, R. Fournier, C. Hourdin, O. Talagrand, M. Collins, S. R. Lewis, P. L. Read, and J.-P. Huot (1999), Improved general circulation models of the Martian atmosphere from the surface to above 80 km, *J. Geophys. Res.*, *104*, 24,155–24,176, doi:10.1029/1999JE001025.

Formisano, V., et al. (2004), PFS: The Planetary Fourier Spectrometer for Mars Express, in *Mars Express: The Scientific Payload*, edited by A. Wilson, *Eur. Space Agency Spec. Publ.*, *ESA SP-1240*, 71–94.

Fritts, D. C., and M. J. Alexander (2003), Gravity dynamics and effects in the middle atmosphere, *Rev. Geophys.*, *41*(1), 1003, doi:10.1029/2001RG000106.

Fritts, D. C., L. Wang, and R. H. Tolson (2006), Mean gravity wave structures and variability in the Mars upper atmosphere inferred from Mars Global Surveyor and Mars Odyssey aerobraking densities, *J. Geophys. Res.*, *111*, A12304, doi:10.1029/2006JA011897.

Hinson, D. P., R. A. Simpson, J. D. Twicken, G. L. Tyler, and F. M. Flasar (1999), Initial results from radio occultation measurements with Mars Global Surveyor, *J. Geophys. Res.*, *104*, 26,997–27,012, doi:10.1029/1999JE001069.

Keating, G. M., et al. (1998), The structure of the upper atmosphere of Mars: In situ accelerometer measurements from Mars Global Surveyor, *Science*, *279*, 1672–1676, doi:10.1126/science.279.5357.1672.

Krasnopolsky, V.-A. (1982), *Photochemestry of the Atmosphere of Mars and Venus*, edited by U. von Zahn, 95 pp., Springer, Berlin.

Krasnopolsky, V. A. (2003), Mapping of Mars O_2 1.27 μm dayglow at four seasonal points, *Icarus*, *165*, 315–325, doi:10.1016/S0019-1035(03)00214-8.

Krasnopolsky, V. A., and G. L. Bjoraker (2000), Mapping of Mars $O_2(^1\Delta)$ dayglow, *J. Geophys. Res.*, *105*(E8), 20,179–20,188, doi:10.1029/2000JE001239.

Krassovsky, V. I. (1957), Nature of the intensity variations of the terrestrial atmospheric emission, *Mem. 8° Soc. Sci. Liege, Quatriéme Ser.*, *18*, 58.

Krassovsky, V. I. (1972), Infrasonic variation of OH emission in the upper atmosphere, *Ann. Geophys.*, *28*, 739.

Langevin, Y., F. Poulet, J.-P. Bibring, and B. Gondet (2005), Sulfates in the North Polar Region of Mars detected by OMEGA/Mars Express, *Science*, *307*(5715), 1584–1586, doi:10.1126/science.1109091.

Lefèvre, F., S. Lebonnois, F. Montmessin, and F. Forget (2004), Three-dimensional modeling of ozone on Mars, *J. Geophys. Res.*, *109*, E07004, doi:10.1029/2004JE002268.

Maltagliati, L., D. V. Titov, T. Encrenaz, R. Melchiorri, F. Forget, H. U. Keller, and J.-P. Bibring (2011), Annual survey of water vapor behavior from the OMEGA mapping spectrometer onboard Mars Express, *Icarus*, *213*(2), 480–495, doi:10.1016/j.icarus.2011.03.030.

Melo, S. M. L., O. Chiu, A. Garzia Munoz, F. Strong, J. C. McConnell, T. G. Salnger, M. J. Taylor, R. P. Lowe, I. C. McDade, and D. L. Huestis (2006), Using airglow measurements to observe gravity waves in the Martian atmosphere, *Adv. Space Res.*, *38*, 730–738, doi:10.1016/j.asr.2005.08.041.

Mlynczak, M. G., and D. J. Nesbitt (1995), The Einstein coefficients for spontaneous emission of the $O_2(a^1\Delta_g)$ state, *Geophys. Res. Lett.*, *22*, 1381–1384, doi:10.1029/95GL01320.

Montabone, L., S. R. Lewis, and P. L. Peter (2005), Interannual variability of Martian dust storms in assimilation of several years of Mars global surveyor observations, *Adv. Space Res.*, *36*, 2146–2155, doi:10.1016/j.asr.2005.07.047.

Nair, H., M. Allen, A. Anbar, Y. Yung, and R. T. Clancy (1994), A photochemical model of the Martian atmosphere, *Icarus*, *111*, 124–150, doi:10.1006/icar.1994.1137.

Newman, S. M., I. C. Lane, A. J. Orr-Ewing, D. A. Newnham, and J. Ballare (1999), Integrated absorption intensity and Einstein coefficients for the O_2 $a^1\Delta_g$-$X^3\Sigma_g^-$ transition: A comparison of cavity ring-down and high resolution Fourier transform spectroscopy with a long-path absorption cell, *J. Chem. Phys.*, *110*, 10,749–10,757, doi:10.1063/1.479018.

Novak, R. E., M. J. Mumma, M. A. DiSanti, N. Dello Russo, and K. Magee-Sauer (2002), Mapping of ozone and water in the atmosphere of Mars near the 1997 Aphelion, *Icarus*, *158*, 14–23, doi:10.1006/icar.2002.6863.

Pettengill, G. H., and P. G. Ford (2000), Winter clouds over the North Martian Polar Cap, *Geophys. Res. Lett.*, *27*(5), 609–612, doi:10.1029/1999GL010896.

Pickersgill, A. O., and G. E. Hunt (1981), An examination of the formation of linear lee waves generated by giant Martian volcanoes, *J. Atmos. Sci.*, *38*, 40–51, doi:10.1175/1520-0469(1981)038<0040:AEOTFO>2.0.CO;2.

Sander, S. P., et al. (2003), Chemical kinetics and photochemical data for use in atmospheric studies, Evaluation numbers 14, *Publ. 02-25*, Jet Propul. Lab., Pasadena, Calif.

Skamarock, W. C., J. B. Klemp, J. Dudhia, D. O. Gill, D. M. Barker, M. Duda, X.-Y. Huang, W. Wang, and J. G. Powers (2008), A description of the advanced research WRF version 3, *NCAR Tech. Note NCAR/TN-475+STR*, Natl. Cent. for Atmos. Res., Boulder, Colo.

Smith, M. D. (2004), Interannual variability in TES atmospheric observations of Mars during 1999–2003, *Icarus*, *167*, 148–165, doi:10.1016/j.icarus.2003.09.010.

Spiga, A., and F. Forget (2009), A new model to simulate the Martian mesoscale and microscale atmospheric circulation: Validation and first results, *J. Geophys. Res.*, *114*, E02009, doi:10.1029/2008JE003242.

Spiga, A., F. Forget, B. Dolla, S. Vinatier, R. Melchiorri, P. Drossart, A. Gendrin, J.-P. Bibring, Y. Langevin, and B. Gondet (2007), Remote sensing of surface pressure on Mars with the Mars Express/OMEGA spectrometer: 2. Meteorological maps, *J. Geophys. Res.*, *112*, E08S16, doi:10.1029/2006JE002870.

Spiga, A., H. Teitelbaum, and V. Zeitlin (2008), Identification and separation of the sources of inertia-gravity waves in the Andes Cordillera region, *Ann. Geophys.*, *26*, 2551–2568, doi:10.5194/angeo-26-2551-2008.

Spiga, A., F. González-Galindo, M. A. Lopez-Valverde, and F. Forget (2012), Gravity waves, cold pockets and CO2 clouds in the Martian mesosphere, *Geophys. Res. Lett.*, *39*, L02201, doi:10.1029/2011GL050343.

Swenson, G. R., and C. S. Gardner (1998), Analytical models for the responses of the mesospheric OH* and Na layers to atmospheric gravity waves, *J. Geophys. Res.*, *103*(D6), 6271–6294, doi:10.1029/97JD02985.

Tarasick, D. W., and O. C. Hines (1990), The observable effect of gravity waves on airglow emission, *Planet. Space Sci.*, *38*, 1105–1119, doi:10.1016/0032-0633(90)90019-M.

Wang, H., and A. P. Ingersoll (2002), Martian clouds observed by Mars Global Surveyor Mars Orbiter Camera, *J. Geophys. Res.*, *107*(E10), 5078, doi:10.1029/2001JE001815.

Zasova, L. V., et al. (2006), Results of measurements with the Planetary Fourier Spectrometer on board Mars Express: Clouds and dust at the end of the Southern summer. A comparison with OMEGA images, *Cosmic Res., Engl. Transl.*, *44*, 305–316, doi:10.1134/S0010952506040046.

Zhu, X., and J. Yee (2007), Wave photochemistry coupling and its effect on water vapor, ozone and airglow variations in the atmosphere of Mars, *Icarus*, *189*, 136–150, doi:10.1016/j.icarus.2007.01.006.